



This is the accepted manuscript made available via CHORUS. The article has been published as:

Traveling-wave electro-optics for microwave-to-optical quantum transduction

Mohan Shen, Manuel C. C. Pace, and Hong X. Tang

Phys. Rev. A **109**, 043515 — Published 16 April 2024

DOI: [10.1103/PhysRevA.109.043515](https://doi.org/10.1103/PhysRevA.109.043515)

Traveling-wave electro-optics for microwave-to-optical quantum transduction

Mohan Shen,¹ Manuel C. C. Pace,¹ and Hong X. Tang^{1,*}

¹*Department of Electrical Engineering, Yale University, New Haven, Connecticut, 06511, USA*

(Dated: March 25, 2024)

High-efficiency microwave-to-optical quantum transduction is crucial for quantum networks and distributed quantum computing. Cavity-based electro-optic transducers have been widely explored due to their cavity-enhanced conversion efficiency, albeit at the compromise of limited transduction bandwidth and strict frequency alignment requirements between microwave and optical modes. A recent advancement in meter-long superconducting electro-optic modulators (SEOM) has demonstrated conversion efficiency approaching that of the cavity-based transducers on a traveling-wave structure while maintaining a broad bandwidth of tens of GHz. This paper provides a further theoretical investigation into the dynamics of the microwave-to-optical conversion process in a traveling-wave geometry. Based on this analysis, we propose a traveling-wave electro-optic transducer design featuring near-unity conversion efficiency and tunable conversion frequency.

I. INTRODUCTION

Large-scale and distributed quantum networks of superconducting quantum computing systems necessitate high-efficiency conversion between microwave and optical frequencies [1, 2]. In the past decades, coherent microwave-to-optical transducers have been extensively studied on various platforms, including cavity electro-optics [3–8], optomagnonics [9–11], optomechanics [12, 13] and atom ensembles [14–17]. Studies on those platforms have universally employed cavity-based transducer design or resonant operation schemes, which enhances the conversion efficiency but limits the conversion bandwidth and conversion frequencies. On the other hand, the very broadband traveling-wave electro-optic modulators (EOMs) have enabled the global internet, but their microwave-to-optical transduction efficiency is only on the order of 1×10^{-7} due to the limited nonlinearity of the electro-optic materials and the short modulation lengths in typical modulator designs [18]. Therefore, traveling-wave transducers have not been widely pursued for high-efficiency microwave-to-optical conversion, despite its advantages of high bandwidth and operational flexibility.

In recent years, the emergence of new electro-optic material platforms with strong Pockels nonlinearity, such as thin-film lithium niobate on insulator (LNOI) [19] and barium titanate integrated into silicon photonics [20, 21], has significantly advanced the performance of electro-optic photonic devices. Integrated electro-optic modulators with V_π of 1 V and bandwidth up to 100 GHz have been demonstrated on LNOI [22]. Micro- and nanostructured barium titanate exhibits a strong Pockels coefficient $r_{42} = 923 \text{ pmV}^{-1}$ [21] and compatibility with cryogenic operations [23]. These novel material platforms have revitalized interest in the potential for traveling-wave electro-optic transduction. As estimated in [18], 5×10^{-2} conversion efficiency entails electro-optic

modulators of V_π 50 mV with 10 dBm optical output power. The recent experimental demonstration of superconducting electro-optic modulator (SEOM) with meter-long modulation length and record-low V_π in the tens of mV range, achieved conversion efficiency of 1×10^{-4} , a 3-orders-of-magnitude improvement over commercial EOMs [24].

However, there will be two major challenges for further advancements to near-unity efficiency with the current SEOM design. First, near-unity efficiency necessitates a modulation length of a few meters while maintaining a low optical propagation length. For such long waveguides, a propagation loss lower than 1 dB/m is desired, which corresponds to quality factors over 30 million. Although it is in principle achievable with the intrinsic lithium niobate material loss limited quality factor of 180 million [25], such low-loss integrated optical component has only been demonstrated on chemical-mechanical polished (CMP) micro-disk resonators [26]. The CMP process is not well suited for ultra-long waveguide fabrication which has more complex design patterns. Second, in the typical traveling-wave electro-optic modulation dispersion scheme, microwave-to-optical transduction happens to both blue and red sidebands, which inherently causes a 50% loss of efficiency. Moreover, cascaded transduction into high-order optical sidebands can occur when the transduction efficiency is high, thus compromising the net efficiency.

In this paper, we propose an interband traveling-wave electro-optic transducer. The scheme is based on the SEOM design that has been reported in [24], but with two optical mode branches and engineered phase matching to enhance the conversion efficiency and prevent conversion into high-order sidebands. This scheme involves two optical mode branches, as shown in Fig. 1(d). By leveraging the strong kinetic inductance of superconductors, microwave dispersion can be engineered to have a slow microwave velocity, which permits phase matched conversion between the two optical mode branches and prohibits conversion into high-order optical modes. We also show that the slowed microwave speed enhances the electro-optic interaction strength and improves the con-

* hong.tang@yale.edu

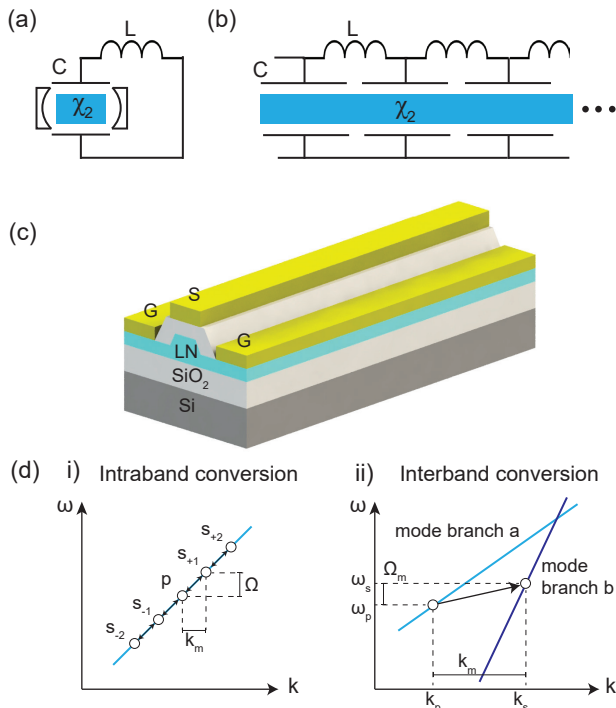


FIG. 1. (a)-(b) Schematic illustration of cavity electro-optics and traveling-wave electro-optics. (c) Material stack and the optical waveguide-electrode design of the traveling-wave electro-optics. (d) i) Intradband electro-optic conversion dispersion. There is only one optical mode branch. Optical pump is set at p point and scattered into multiple sidebands. (d) ii) Interband electro-optic conversion dispersion. There are two optical mode branches with mode crossing. The pump is set at k_p of mode branch a. The phase-matched microwave with wave vector k_m is converted into optical mode branch b.

version efficiency. It is worth noting slowed microwave transmission lines are commonly exploited in superconducting circuits and thus do not present a particular challenge to implement [27]. This paper is organized as follows. In Sec. II, we present the theoretical description of the temporal and spatial dynamics of the traveling-wave electro-optic interaction. In Sec. III, we calculate the conversion efficiency based on the theoretical results and numerically simulated mode profiles and dispersion.

II. THEORETICAL DESCRIPTION

Derivation of the traveling-wave electro-optic Hamiltonian follows the one done in reference [24], and is restated in the Appendix A of this paper. Here, the main text presents the phase-matching conditions and discusses the theoretical solutions under specific conditions.

A. Dispersion and phase matching

Here we consider two different dispersion schemes as shown in Fig. 1(d) i) and ii). In Fig. 1(d) i), the dispersion relation corresponds to that of a conventional traveling-wave electro-optic modulator [22], where there is only one optical mode branch. In this situation, which we call intraband conversion, the pump and converted sidebands are on the same mode branch. The phase-matching requirement in this case is straightforward, where the slope of the dispersion curve for the microwave and optical signals need to be identical, and this is also known as velocity matching in electro-optic modulator design. Note that this phase-matching condition allows cascaded electro-optic transduction into higher-order sidebands. The dispersion curves shown in Fig. 1(d) ii) are what we propose for coherent microwave-to-optical conversion, which involves two optical mode branches with mode crossing. When a parametric pump is applied at frequency ω_p of optical mode a near the mode crossing point, the phase-matched microwave frequency Ω_m and optical frequency ω_s on mode branch b must satisfy:

$$k_p + k_m = k_s, \quad (1a)$$

$$\omega_p + \Omega_m = \omega_s. \quad (1b)$$

This phase-matching scheme is inherently single-sideband. Also, due to the traveling wave's continuous spectrum, the phase-matched microwave frequency is tunable by adjusting the pump light frequency. As shown in Fig. 1(d) ii), for a given microwave, we can always find the optical pump such that their sum ends up on mode branch b. If the microwave frequency is detuned from the perfect phase-matched frequency by Δ to $\Omega_m + \Delta$, the converted optical frequency on mode branch b will be $\omega_s + \Delta$. The corresponding wave vector mismatch is

$$k'(\Delta) = k_a(\omega_p) - k_b(\omega_s + \Delta) + k_c(\Omega_m + \Delta). \quad (2)$$

The impact of this phase mismatch on the microwave-to-optical conversion will be discussed later in the next section.

Note that the group velocities of the traveling microwave in the intraband and interband conversion are different: in the intraband case, the microwave velocity matches that of the optics; while in the interband case, the microwave velocity is engineered to be much slower than that of the optics. It is shown in Sec. III that the slow microwave can be realized by utilizing the kinetic inductance of the superconductor microwave transmission line. This slow microwave dispersion can improve the coupling strength between microwave and optics, as elaborated in the next section.

B. Dynamic Equations and Solutions

The general-case Heisenberg equations of motion are given by Eq. (A17). In a practical experimental condi-

tion, the pump is a constant laser input with strong intensity to boost the electro-optic conversion efficiency. Because of its much stronger intensity than that of the signal light and microwave, the back-action of the electro-optic interaction on the pump is negligible and the pump can be taken as a classical light source. In the steady-state,

$$A(z, t) = \alpha_p e^{-\frac{\kappa_a}{2v_a} z}, \quad (3)$$

where α_p is a constant and the exponential decay term indicates the dissipation in the optical waveguide of mode a , where κ_a is the intrinsic dissipation and v_a is the group velocity. Suppose that at $z = 0$ the pump power is P_{in} , then $P_{in} = v_a \hbar \omega_p |\alpha_p|^2$. If the phase of the pump is set to be 0,

$$\alpha_p = \sqrt{\frac{P_{in}}{v_a \hbar \omega_p}}. \quad (4)$$

Considering the phase mismatch in Eq. (2) and the negligible back-action on A , the temporal-spatial dynamic equations of Eq. (A17) become:

$$\frac{\partial B}{\partial t} + v_b \frac{\partial B}{\partial z} = -\frac{\kappa_b}{2} B - i g_0 \alpha_p e^{-\frac{\kappa_a}{2v_a} z} C e^{ik'(\Delta)z}, \quad (5a)$$

$$\frac{\partial C}{\partial t} + v_c \frac{\partial C}{\partial z} = -\frac{\kappa_c}{2} C - i g_0^* \alpha_p^* e^{-\frac{\kappa_a}{2v_a} z} B e^{-ik'(\Delta)z}, \quad (5b)$$

where g_0 is given by Eq. (A14), κ_l and v_l ($l = a, b$ or c) are the intrinsic dissipation rates and group velocities respectively for the three modes.

In the steady-state, the temporal derivative terms in Eq. (5) equal to zero. We also further assume that the intensity of the pump light does not decay along the interaction length L , i.e. $\kappa_a = 0$. This is approximately true for low loss photonic waveguide within tens of cm length [28]. Under this undepleted pump assumption, the steady-state Heisenberg equation and its solution is given in Appendix B. We firstly assume perfect phase match $k'(\Delta) = 0$, and the boundary conditions $B = 0$ and $C = C_0$ at $z = 0$. Then, in the regime $|\gamma| \gg \left| \frac{\kappa_b}{v_b} - \frac{\kappa_c}{v_c} \right|$, the solution Eq. (B2) can be simplified to

$$B = -i C_0 e^{i \arg(\gamma)} \sqrt{\frac{v_c}{v_b}} e^{-\left(\frac{\kappa_b}{2v_b} + \frac{\kappa_c}{2v_c}\right) \frac{z}{2}} \sin(|\gamma|z), \quad (6a)$$

$$C = C_0 e^{-\left(\frac{\kappa_b}{2v_b} + \frac{\kappa_c}{2v_c}\right) \frac{z}{2}} \cos(|\gamma|z), \quad (6b)$$

where $\gamma = \frac{g_0 \alpha_p}{\sqrt{v_b v_c}}$. The conversion efficiency can be given as

$$\eta = \frac{v_b |B|^2}{v_c |C_0|^2} = e^{-\left(\frac{\kappa_b}{2v_b} + \frac{\kappa_c}{2v_c}\right) z} \sin^2(|\gamma|z), \quad (7)$$

which is the output optical photon flux over the input microwave photon flux.

This result indicates that with a strong pump, the microwave-to-optical photon conversion happens periodically in space and a complete quantum state transfer

happens after a length of $l = \frac{\pi}{2|\gamma|}$. Under the present assumption that $|\gamma| \gg \left| \frac{\kappa_b}{v_b} - \frac{\kappa_c}{v_c} \right|$, the above shows that the loss term becomes the average of the two modes. Intuitively, this stems from the periodic transfer of energy from one mode to the other. Note that the assumption above on $|\gamma|$ is compared with the difference of the two propagation loss terms, which makes no assumption on the strength of γ compared to either of the two terms.

In the phase-mismatched condition, where $k' \neq 0$, we assume $\kappa_b = \kappa_c = 0$ to examine the impact of phase mismatch. In this case the solution is reduced to:

$$B = -i C_0 \sqrt{\frac{v_c}{v_b}} e^{i \frac{k'}{2} z} \frac{\gamma}{\beta} \sin(\beta z), \quad (8a)$$

$$C = C_0 e^{-i \frac{k'}{2} z} \left(\cos(\beta z) + \frac{i k'}{\beta} \sin(\beta z) \right), \quad (8b)$$

where $\beta = \sqrt{|\gamma|^2 + k'^2/4}$. From the above, one can derive that the phase-mismatched maximum conversion efficiency is $\eta = |\gamma|^2/\beta^2 = 1/(1 + k'^2/4|\gamma|^2)$. Due to the phase mismatch, the oscillation period is shorter and the conversion is suppressed by a factor of $|\gamma|^2/\beta^2$. This spatial phase mismatched result is analogous to temporal frequency mismatched Rabi oscillations.

III. REALIZATION ON LITHIUM NIOBATE PLATFORM

In this section we numerically simulate the microwave-to-optical conversion efficiency of the proposed traveling-wave transducer implemented on the LNOI platform, which has large electro-optic coefficients, low optical loss, and tight optical confinement [28, 29]. The microwave transmission line is made from superconductor niobium nitride (NbN), which has a high transition temperature and high kinetic inductance [30]. The high kinetic inductance of thin-film NbN can be utilized to engineer the microwave dispersion and improve the electro-optic coupling strength as shown in Sec. III B.

A. Optical and Microwave Dispersion

To produce the dispersion shown in Fig. 1(d) ii), two optical modes with mode crossing are required. Mode crossing happens between optical modes of different polarization in a birefringent optical waveguide. Given the electro-optic coefficient tensor of lithium niobate [29], we can utilize r_{42} , r_{51} or r_{61} elements to realize conversion between two optical modes of different polarization. To utilize the larger electro-optic coefficients of $r_{42} = r_{51} = 33$ pm/V, we consider the conversion between TM and TE modes on X-cut LNOI, and the electric field is applied vertically along the crystalline X direction. In this case, coplanar microwave transmission line can be employed with the signal electrode placed on top of the waveguide cladding to generate an electric field in the

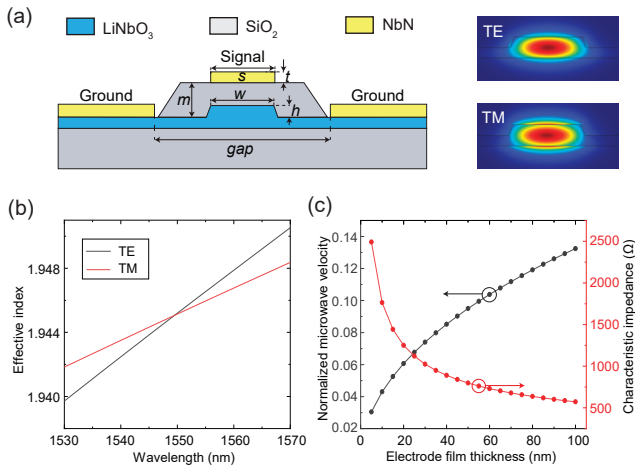


FIG. 2. (a) Cross section of optical waveguide and microwave transmission line. The X-cut lithium niobate film is on silicon dioxide on silicon. The mode profile of TE and TM mode are shown on the right side. (b) Optical mode dispersion of the TE and TM modes. In this simulation, the lithium niobate film thickness is 615 nm, $h=315$ nm, $w=2$ μm and $m=1.5$ μm . (c) Microwave impedance and velocity. In this simulation, the signal electrode width $s=0.5$ μm , $gap=6$ μm and the NbN film thickness t is varied to tune the microwave velocity and impedance. We use 50 pH/square kinetic inductance for the 10 nm-thick NbN film. The normalized microwave speed is normalized by the speed of light in vacuum.

vertical direction. The schematic cross section is illustrated in Fig 2(a), where a half-etched optical waveguide is electro-optically coupled with a coplanar microwave transmission line.

Optical and microwave modes are simulated using COMSOL. With the geometric parameters specified in the caption of Fig. 2, there is a mode crossing between fundamental TM and TE mode at around 1550 nm. The mode profile of these two modes are shown in Fig. 2(a) and their simulated dispersion near the mode crossing is shown in Fig. 2(b). In the coplanar superconducting microwave transmission line simulation, the kinetic inductance is taken into account, which can be engineered by changing the superconductor film thickness or the signal electrode width [31]. From the simulated results shown in Fig. 2(c), we see that the microwave velocity can be effectively slowed down by increasing the kinetic inductance through reducing the film thickness. The microwave speed can be decreased to as low as a few percent of the light speed in vacuum. The slower microwave also boosts the conversion efficiency as suggested by Eq. 7. Actually, the characteristic impedance increases as the microwave velocity decreases in our simulation with swept film thickness, as shown in Fig. 2(c). This is because in microwave transmission line design, its impedance $Z = \sqrt{L/C}$ and velocity $v = \sqrt{1/LC}$, where L and C are the specific inductance and capacitance. By only sweeping the film thickness, the specific capacitance C does not change significantly, but the kinetic

inductance is tuned dramatically. As a result, decreasing the velocity amounts to increasing the impedance. Impedance matching between a 50 Ω input and the device can be achieved by the design and fabrication of a taper on chip [32]. For low RF reflection at all frequencies above a threshold, a Klopfenstein taper can be used.

B. Numerical Simulation of Conversion Efficiency

We calculate the coupling strength by inserting the simulated optical and microwave mode profiles into Eq. A14. The conversion efficiency is then computed by Eq. 6. Here we assume an undepleted optical pump power of 20 dBm at telecom wavelength ($\omega_p = 200$ THz), $\kappa_b = 10$ MHz and $v_b = c/2$ (optical propagation loss of 1.5 dB/m, or equivalently 20 million intrinsic quality factor). We also assume $\Omega = 10$ GHz, $\kappa_c = 0.5$ MHz (intrinsic quality factor of 20 k) and v_c is varied in the calculation by tuning the film thickness according to Fig 2(c). The result is shown in Fig. 3. With a thick film and low microwave impedance of 200 Ohm, it takes about a 2 meter-long modulation length to reach peak conversion efficiency of about 50%. However with thinner film of about 5 nm and therefore higher microwave impedance at 2500 Ohm, the optimal modulation length is reduced to about 0.6 m and the peak conversion efficiency increases to about 80%. It should be noted here that a practical demonstration of quantum signal transduction at temperatures below 100 mK would make use of a device operating in a pulsed regime [33]. Considering the balance between optical power consumption and the cooling power of dilution fridge systems, duty cycles on the order of 1% should be suitable.

Here, the assumed optical propagation loss is close to the state-of-the-art reported on integrated LNOI using conventional fabrication process and well within the material's intrinsic loss. The thinnest NbN film thickness we assume is 5 nm at width of $s=0.5$ μm . We believe the assumed 20 k quality factor is reasonable given the reported 4 k quality factor of a 4 nm-thick resonator with only 23 nm-wide nano-wire inductor [30]. Note that electro-optic materials like barium titanate possess a one-order-of-magnitude higher nonlinear coefficient. With future enhancement on the material preparation and low-loss fabrication process, it is possible to reduce the modulation length for near-unity efficiency to a few centimeters, close to that of the conventional EOMs.

IV. CONCLUSION

In this paper, we present an interband traveling-wave electro-optic transduction scheme, which allows coherent microwave-to-optical conversion without possible excitations to higher-order sidebands. This interband phase-matching condition also allows the conversion of selected microwave frequency by adjusting the pump light wave-

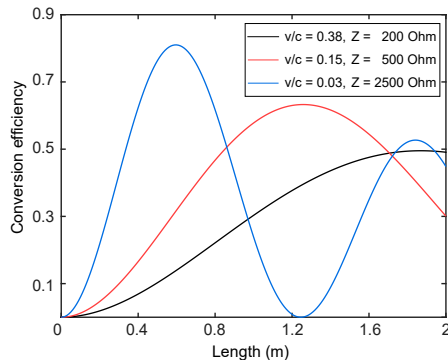


FIG. 3. Conversion efficiency with different microwave velocity and impedance. With a high impedance of 2500 Ohm, the highest conversion efficiency of about 80% is achieved with only 0.6 meter-long modulation length.

length. Our analysis shows that under a strong pump light, the microwave-to-optical conversion occurs periodically in space. The fundamental limit on the conversion efficiency is the electro-optic nonlinear coefficient and the optical and microwave losses of the material platform. We perform numerical simulation and calculation to show that near-unity conversion efficiency is achievable on the LNOI and NbN material platform with appropriate material parameters.

ACKNOWLEDGMENTS

This project is funded by DOE Office of Science, National Quantum Information Science Research Centers, Co-design Center for Quantum Advantage (C2QA), Contract No. DE-SC0012704.

Appendix A: Traveling-wave Electro-optic Hamiltonian

Based on previous theoretical works on quantum description of traveling wave systems [34–36], we derive the dynamic equations of the electro-optic system through its Hamiltonian, which captures the spatial and temporal variance, electro-optic coupling and phase mismatch. If we consider the dispersion situation illustrated in Fig. 1(d) ii), the system can be described by Hamiltonian

$$H = H_a + H_b + H_c + H_V, \quad (\text{A1})$$

where H_a , H_b and H_c are the Hamiltonian for the two optical mode branches and the microwave respectively and H_V is the electro-optic coupling term.

The electric field of these three modes can be expressed in terms of the continuous mode creation and annihilation operators [34],

$$\mathbf{E}_l = \int \frac{l(k)\mathbf{u}_{lk}(x, y)e^{ikz} + H.c.}{\sqrt{4\pi \int \epsilon_{l,i}u_{lk,i}u_{l,i}^* dx dy / \hbar \Omega(k)}} dk, \quad (\text{A2})$$

where $l(k)$ is the continuous mode annihilation operator, $\epsilon_{l,i}$ are the three components of the material permittivity, and $\mathbf{u}_{lk}(x, y) = u_{lk,i}(x, y)\mathbf{e}_i$. In the above, $l = a, b$ or c and $i = x, y$ or z and Einstein summation convention over i is applied. Here $\mathbf{u}_{lk}(x, y)$ is the electric field mode profile of each mode at wave vector k . The denominators in the equation are for normalization purposes and will disappear in the expression of later Hamiltonian. The commutation relations of the continuous annihilation and creation operators reads below [34]:

$$[l(k), l'(k')] = 0, [l(k), l'^{\dagger}(k')] = \delta_{ll'}\delta(k - k'). \quad (\text{A3})$$

Still $l = a, b$ or c . With Eq. (A2) and neglecting vacuum fluctuations, the Hamiltonian of each mode branch is

$$\begin{aligned} H_l &= \int \epsilon_{l,i} E_{l,i} E_{l,i}^* dx dy dz \\ &= \int \hbar \omega_l(k) l^{\dagger}(k) l(k) dk. \end{aligned} \quad (\text{A4})$$

In Eq. (A4), the $\frac{1}{2}$ factor of the electric field energy density is multiplied by 2 to account for the magnetic field energy as the electric field and the magnetic field have the same amount of energy.

With the continuous mode operators, a wave packet in a given mode branch can be mathematically expressed by the envelope operator [35, 36] around a chosen frequency ω . This is defined as

$$\tilde{A}_{\omega}(z) = \frac{1}{\sqrt{2\pi}} \int a_k e^{i(k - k_a(\omega))z} dk, \quad (\text{A5})$$

where $\tilde{A}_{\omega}(z)$ is the envelope operator of the wave packet in mode branch a , with continuous mode annihilation operators a_k , dispersion relation $k_a(\omega)$, and the chosen central frequency ω . Through inverse Fourier transformation, we have

$$a_k = \frac{1}{\sqrt{2\pi}} \int \tilde{A}_{\omega}(z) e^{-i(k - k_a(\omega))z} dz. \quad (\text{A6})$$

The commutation relation of the envelope operators can be derived from the commutation relation of the continuous creation and annihilation operators in Eq. (A3), which gives

$$[\tilde{A}_{\omega}(z), \tilde{A}_{\omega'}(z')] = 0, \quad (\text{A7a})$$

$$[\tilde{A}_{\omega}(z), \tilde{A}_{\omega'}^{\dagger}(z')] = e^{i(k_a(\omega') - k_a(\omega))z} \delta(z - z'). \quad (\text{A7b})$$

We use \tilde{A} , \tilde{B} and \tilde{C} to represent the envelope operator of mode a , b and c . Substituting Eq. (A6) to Eq. (A4) and using the Taylor expansion of $\omega_a(k)$ around $k_a(\omega)$ giving

$\omega_a(k) = \sum_{n=0}^{\infty} \frac{1}{n!} \left. \frac{\partial^n \omega_a}{\partial k^n} \right|_{\omega} (k - k_a(\omega))^n$, the Hamiltonian for mode branch a becomes

$$H_a = \int \hbar \tilde{A}_{\omega}^{\dagger}(z) \left(\sum_{n=0}^{\infty} \frac{1}{n!} \left. \frac{\partial^n \omega_a}{\partial k^n} \right|_{\omega} \left(-i \frac{\partial}{\partial z} \right)^n \tilde{A}_{\omega}(z) \right) dz. \quad (\text{A8})$$

To arrive at the equation above we use the Fourier transform identity

$$\int (ik)^n f(x) e^{ikx} dk dx = \int \frac{\partial^n f(x)}{\partial x^n} e^{ikx} dk dx. \quad (\text{A9})$$

The integration in the definition of the envelope operators is over all the wavenumber, physically, this means that the envelope operator represents the photons in all the frequency range. In real experiments, however, we are interested in bandwidths where the dispersion relation can be approximated as linear. In this linear dispersion wave packet assumption, the Hamiltonian can be simplified as Eq. (A10):

$$H_a = \int (\hbar \omega \tilde{A}_{\omega}^{\dagger}(z) \tilde{A}_{\omega}(z) - i \hbar v_a \tilde{A}_{\omega}^{\dagger}(z) \frac{\partial \tilde{A}_{\omega}(z)}{\partial z}) dz, \quad (\text{A10})$$

where v_a is the group velocity at frequency ω for mode branch a . The first term is only exact if the signal is monochromatic at ω , and $\tilde{A}^{\dagger}(z, \omega) \tilde{A}(z, \omega)$ would then be the photon number density. The second term is the correction for other frequencies under the linear dispersion assumption. The Hamiltonian for mode branches b and c , H_b and H_c can also be expressed using the envelope operators in the same form. Using the commutation relation Eq. (A7), we can get the Heisenberg equation of motion in terms of the envelope operators

$$\begin{aligned} \frac{\partial \tilde{A}_{\omega}(z)}{\partial t} &= \frac{1}{i\hbar} [\tilde{A}_{\omega}(z), H_a] \\ &= -i\omega \tilde{A}_{\omega}(z) - v_a \frac{\partial \tilde{A}_{\omega}(z)}{\partial z}. \end{aligned} \quad (\text{A11})$$

Now consider the interaction term in the system Hamiltonian which can be expressed as [4]

$$H_V = \frac{1}{2} \int r_{ijk} \epsilon_{a,i} \epsilon_{b,j} E_{a,i} E_{b,j} E_{c,k} dx dy dz, \quad (\text{A12})$$

where a, b and c denote the different mode branches and r_{ijk} is the electro-optic component. In Eq. (A2) the electric field mode profile $u_{lk}(x, y)$ is a function of the wavelength, but within a narrow frequency range, it is a good assumption that the mode profile does not change. In addition, the narrow frequency range can also be used to approximate $\omega_l(k)$ from the normalization factor as ω_l (δk terms would combine with the integrals in k_i to give higher order terms). Given this, substitute Eq. (A2) into H_V and keep only the electro-optic conversion terms of

interests, we have

$$H_V = \int \left(\frac{\hbar g_0 e^{ik'z}}{(2\pi)^{\frac{3}{2}}} a(k_1) b^{\dagger}(k_2) c(k_3) + H.c. \right) dk_1 dk_2 dk_3 dz, \quad (\text{A13})$$

$$\hbar g_0 = \frac{1}{4\sqrt{2}} \frac{\int r_{ijk} \epsilon_{a,i} \epsilon_{b,j} u_{a,i} u_{b,j}^* u_{c,k} dx dy}{\prod_{l=a,b,c} \sqrt{\int \epsilon_{l,i} u_{l,i} u_{l,i}^* dx dy} / \hbar \omega_l} \quad (\text{A14})$$

where $k' = k_1 - k_2 + k_3$. As shown in Fig. 1 c) ii), suppose that the central frequency of the wave packets of mode a, b and c are ω_p, ω_s and Ω respectively, then Eq. (A13) can be written in terms of envelope operators as

$$H_V = \int \left(\hbar g_0 \tilde{A}_{\omega_p}(z) \tilde{B}_{\omega_s}^{\dagger}(z) \tilde{C}_{\Omega}(z) e^{ik'z} + H.c. \right) dz, \quad (\text{A15})$$

where $k' = k_a(\omega_p) - k_b(\omega_s) + k_c(\Omega)$ is the phase mismatch term between wave packet center frequencies.

Knowing the interaction Hamiltonian, the interaction term in the Heisenberg equations of motion are obtained in the same way as for the free propagation term in Eq. (A11). This gives the two-operator terms in Eq. (A16a) to (A16c). In the following, the loss rate of each mode was also added with κ_l factors. In the bandwidth considered, these rates are considered to be location and frequency independent. Mathematically, they have no impact on the above calculations and are obtained by generalizing to complex frequencies (replacing $\omega = \omega_l(k) + i\kappa_l/2$). The system of dynamic equations then reads:

$$\frac{\partial \tilde{A}}{\partial t} = -(i\omega_p + \frac{\kappa_a}{2}) \tilde{A} - v_a \frac{\partial \tilde{A}}{\partial z} - ig_0^* \tilde{B} \tilde{C}^{\dagger} e^{-ik'z}, \quad (\text{A16a})$$

$$\frac{\partial \tilde{B}}{\partial t} = -(i\omega_s + \frac{\kappa_b}{2}) \tilde{B} - v_b \frac{\partial \tilde{B}}{\partial z} - ig_0 \tilde{A} \tilde{C} e^{ik'z}, \quad (\text{A16b})$$

$$\frac{\partial \tilde{C}}{\partial t} = -(i\Omega + \frac{\kappa_c}{2}) \tilde{C} - v_c \frac{\partial \tilde{C}}{\partial z} - ig_0^* \tilde{A}^{\dagger} \tilde{B} e^{-ik'z} \quad (\text{A16c})$$

To get rid of the fast oscillating component in \tilde{A}, \tilde{B} and \tilde{C} , we introduce their rotating frame equivalent $A = \tilde{A}_{\omega_p} e^{i\omega_p t}$, $B = \tilde{B}_{\omega_s} e^{i\omega_s t}$ and $C = \tilde{C}_{\Omega} e^{i\Omega t}$. Replacing them into Eq. (A16), \tilde{A}, \tilde{B} and \tilde{C} are replaced by A, B and C and the fast oscillating terms on the right hand side of Eq. (A16) disappear:

$$\frac{\partial A}{\partial t} = -\frac{\kappa_a}{2} A - v_a \frac{\partial A}{\partial z} - ig_0^* B C^{\dagger} e^{-ik'z}, \quad (\text{A17a})$$

$$\frac{\partial B}{\partial t} = -\frac{\kappa_b}{2} B - v_b \frac{\partial B}{\partial z} - ig_0 A C e^{ik'z}, \quad (\text{A17b})$$

$$\frac{\partial C}{\partial t} = -\frac{\kappa_c}{2} C - v_c \frac{\partial C}{\partial z} - ig_0^* A^{\dagger} B e^{-ik'z}. \quad (\text{A17c})$$

Up to this point, perfect frequency matching ($\omega_s = \omega_p + \Omega$) has not been required. One could have selected $\omega_s + \Delta$ instead of ω_s for mode branch b 's envelope operator and associated rotating frame. In the above, we can therefore simply replace the phase mismatch k' with its expression given in Eq. 2.

Appendix B: Dynamic equations solution

The steady-state Heisenberg equation under the undepleted pump assumption can be written as:

$$\frac{\partial B}{\partial z} = -\frac{\kappa_b}{2v_b}B - i\frac{g_0\alpha_p}{v_b}Ce^{ik'(\Delta)z}, \quad (\text{B1a})$$

$$\frac{\partial C}{\partial z} = -\frac{\kappa_c}{2v_c}C - i\frac{g_0^*\alpha_p^*}{v_c}Be^{-ik'(\Delta)z}, \quad (\text{B1b})$$

which has solutions:

$$B = e^{-\frac{\kappa_b}{2v_b}z}(C_1e^{\beta_1z} + C_2e^{\beta_2z}), \quad (\text{B2a})$$

$$C = -\frac{v_b}{ig_0\alpha_p}e^{-\frac{\kappa_c}{2v_c}z}(C_1\beta_1e^{-\beta_2z} + C_2\beta_2e^{-\beta_1z}), \quad (\text{B2b})$$

where

$$\beta = \frac{\kappa_b}{2v_b} - \frac{\kappa_c}{2v_c} + ik'(\Delta), \quad (\text{B3a})$$

$$\beta_1 = \frac{\beta + \sqrt{\beta^2 - 4\frac{|g_0\alpha_p|^2}{v_bv_c}}}{2}, \quad (\text{B3b})$$

$$\beta_2 = \frac{\beta - \sqrt{\beta^2 - 4\frac{|g_0\alpha_p|^2}{v_bv_c}}}{2}, \quad (\text{B3c})$$

and C_1 and C_2 are two constants determined according to boundary conditions.

Appendix C: Transduction bandwidth

In this section we estimate the transduction bandwidth of our proposed conversion scheme. As shown in Eq. (8a), the effect of phase mismatch arise from the non-zero k' in the $\beta = \sqrt{|\gamma|^2 + k'^2/4}$ term. We can define the bandwidth as the frequency detuning Δ such that $k'(\Delta) = 2\gamma$. Given Eq. (1a) and (2),

$$k'(\Delta) = \left(\frac{1}{v_b} - \frac{1}{v_c}\right)\Delta. \quad (\text{C1})$$

Taking the simulated condition in Fig 3 as an example, where optical velocity $v_b = 0.5c$, microwave velocity $v_c = 0.03c$ and an about 80% conversion efficiency is achieved at 0.6 m, the corresponding frequency detuning is $\Delta = \pm 50$ MHz, and therefore, the bandwidth is about 100 MHz.

-
- [1] N. J. Lambert, A. Rueda, F. Sedlmeir, and H. G. L. Schwefel, Coherent Conversion Between Microwave and Optical Photons—An Overview of Physical Implementations, *Advanced Quantum Technologies* **3**, 1900077 (2020).
- [2] X. Han, W. Fu, C.-L. Zou, L. Jiang, and H. X. Tang, Microwave-optical quantum frequency conversion, *Optica* **8**, 1050 (2021).
- [3] M. Tsang, Cavity quantum electro-optics, *Phys. Rev. A* **81**, 063837 (2010).
- [4] L. Fan, C.-L. Zou, R. Cheng, X. Guo, X. Han, Z. Gong, S. Wang, and H. X. Tang, Superconducting cavity electro-optics: A platform for coherent photon conversion between superconducting and photonic circuits, *Science Advances* **4**, eaar4994 (2018).
- [5] T. P. McKenna, J. D. Witmer, R. N. Patel, W. Jiang, R. Van Laer, P. Arrangoiz-Arriola, E. A. Wollack, J. F. Herrmann, and A. H. Safavi-Naeini, Cryogenic microwave-to-optical conversion using a triply resonant lithium-niobate-on-sapphire transducer, *Optica* **7**, 1737 (2020), arXiv:2005.00897.
- [6] J. Holzgrafe, N. Sinclair, D. Zhu, A. Shams-Ansari, M. Colangelo, Y. Hu, M. Zhang, K. K. Berggren, and M. Lončar, Cavity electro-optics in thin-film lithium niobate for efficient microwave-to-optical transduction, *Optica* **7**, 1714 (2020).
- [7] Y. Xu, A. A. Sayem, L. Fan, C.-L. Zou, S. Wang, R. Cheng, W. Fu, L. Yang, M. Xu, and H. X. Tang, Bidirectional interconversion of microwave and light with thin-film lithium niobate, *Nat. Commun.* **12**, 4453 (2021).
- [8] W. Hease, A. Rueda, R. Sahu, M. Wulf, G. Arnold, H. G. Schwefel, and J. M. Fink, Bidirectional electro-optic wavelength conversion in the quantum ground state, *PRX Quantum* **1**, 020315 (2020).
- [9] X. Zhang, N. Zhu, C.-L. Zou, and H. X. Tang, Optomagnonic Whispering Gallery Microresonators, *Phys. Rev. Lett.* **117**, 123605 (2016), arXiv:1510.03545.
- [10] R. Hisatomi, A. Osada, Y. Tabuchi, T. Ishikawa, A. Noguchi, R. Yamazaki, K. Usami, and Y. Nakamura, Bidirectional conversion between microwave and light via ferromagnetic magnons, *Physical Review B* **93**, 174427 (2016), arXiv:1601.03908.
- [11] N. Zhu, X. Zhang, X. Han, C.-L. Zou, C. Zhong, C.-H. Wang, L. Jiang, and H. X. Tang, Waveguide cavity optomagnonics for microwave-to-optics conversion, *Optica* **7**, 1291 (2020).
- [12] R. W. Andrews, R. W. Peterson, T. P. Purdy, K. Cicak, R. W. Simmonds, C. A. Regal, and K. W. Lehnert, Bidirectional and efficient conversion between microwave and

- optical light, *Nat. Phys.* **10**, 321 (2014), [arXiv:1310.5276](#).
- [13] M. Mirhosseini, A. Sipahigil, M. Kalaei, and O. Painter, Quantum transduction of optical photons from a superconducting qubit, *arXiv preprint arXiv:2004.04838* (2020).
- [14] K. V. Adwaith, A. Karigowda, C. Manwatkar, F. Bretenaker, and A. Narayanan, Coherent microwave-to-optical conversion by three-wave mixing in a room temperature atomic system, *Opt. Lett.* **44**, 33 (2019).
- [15] T. Vogt, C. Gross, J. Han, S. B. Pal, M. Lam, M. Kiffner, and W. Li, Efficient microwave-to-optical conversion using Rydberg atoms, *Phys. Rev. A* **99**, 023832 (2019), [arXiv:1810.09722](#).
- [16] H.-T. Tu, K.-Y. Liao, Z.-X. Zhang, X.-H. Liu, S.-Y. Zheng, S.-Z. Yang, X.-D. Zhang, H. Yan, and S.-L. Zhu, High-efficiency coherent microwave-to-optics conversion via off-resonant scattering, *Nat. Photonics* **16**, 291 (2022).
- [17] S. Borówka, U. Pylypenko, M. Mazelanik, and M. Parniak, Continuous wideband microwave-to-optical converter based on room-temperature Rydberg atoms, *Nat. Photonics* **10.1038/s41566-023-01295-w** (2023).
- [18] A. Youssefi, I. Shomroni, Y. J. Joshi, N. Bernier, A. Lukashchuk, P. Urich, L. Qiu, and T. J. Kippenberg, Cryogenic electro-optic interconnect for superconducting devices, *arXiv preprint* (2020), [arXiv:2004.04705](#).
- [19] C. Wang, M. Zhang, B. Stern, M. Lipson, and M. Lončar, Nanophotonic lithium niobate electro-optic modulators, *Optics Express* **26**, 1547 (2018).
- [20] F. Eltes, D. Caimi, F. Fallegger, M. Sousa, E. O'Connor, M. D. Rossell, B. Offrein, J. Fompeyrine, and S. Abel, Low-Loss BaTiO₃-Si Waveguides for Nonlinear Integrated Photonics, *ACS Photonics* **3**, 1698 (2016).
- [21] S. Abel, F. Eltes, J. E. Ortmann, A. Messner, P. Castera, T. Wagner, D. Urbonas, A. Rosa, A. M. Gutierrez, D. Tulli, P. Ma, B. Baeuerle, A. Josten, W. Heni, D. Caimi, L. Czornomaz, A. A. Demkov, J. Leuthold, P. Sanchis, and J. Fompeyrine, Large Pockels effect in micro- and nanostructured barium titanate integrated on silicon, *Nature Materials* **18**, 42 (2019).
- [22] C. Wang, M. Zhang, X. Chen, M. Bertrand, A. Shams-Ansari, S. Chandrasekhar, P. Winzer, and M. Lončar, Integrated lithium niobate electro-optic modulators operating at CMOS-compatible voltages, *Nature* **562**, 101 (2018).
- [23] F. Eltes, G. E. Villarreal-Garcia, D. Caimi, H. Siegwart, A. A. Gentile, A. Hart, P. Stark, G. D. Marshall, M. G. Thompson, J. Barreto, J. Fompeyrine, and S. Abel, An integrated optical modulator operating at cryogenic temperatures, *Nature Materials* **19**, 1164 (2020).
- [24] M. Shen, J. Xie, Y. Xu, S. Wang, R. Cheng, W. Fu, Y. Zhou, and H. X. Tang, Photonic link from single-flux-quantum circuits to room temperature, *Nat. Photonics* **10.1038/s41566-023-01370-2** (2024).
- [25] A. Shams-Ansari, G. Huang, L. He, Z. Li, J. Holzgrafe, M. Jankowski, M. Churaev, P. Kharel, R. Cheng, D. Zhu, N. Sinclair, B. Desiatov, M. Zhang, T. J. Kippenberg, and M. Lončar, Reduced material loss in thin-film lithium niobate waveguides, *APL Photonics* **7**, 10.1063/5.0095146 (2022).
- [26] R. Gao, H. Zhang, F. Bo, W. Fang, Z. Hao, N. Yao, J. Lin, J. Guan, L. Deng, M. Wang, L. Qiao, and Y. Cheng, Broadband highly efficient nonlinear optical processes in on-chip integrated lithium niobate microdisk resonators of Q-factor above 10⁸, *New J. Phys.* **23**, 123027 (2021).
- [27] R. Cheng, Y. Zhou, S. Wang, M. Shen, T. Taher, and H. X. Tang, A 100-pixel photon-number-resolving detector unveiling photon statistics, *Nature Photonics* **17**, 112 (2023).
- [28] X. Zhu, Y. Hu, S. Lu, H. K. Warner, X. Li, Y. Song, L. Magalhaes, A. Shams-Ansari, N. Sinclair, and M. Loncar, Twenty-nine million intrinsic q-factor monolithic microresonators on thin film lithium niobate (2024), [arXiv:2402.16161 \[physics.optics\]](#).
- [29] R. S. Weis and T. K. Gaylord, Lithium niobate: Summary of physical properties and crystal structure, *Applied Physics A Solids and Surfaces* **37**, 191 (1985).
- [30] M. Xu, R. Cheng, Y. Wu, G. Liu, and H. X. Tang, Magnetic Field-Resilient Quantum-Limited Parametric Amplifier, *PRX Quantum* **4**, 010322 (2023).
- [31] J. W. Baker, J. D. Lejeune, and D. G. Naugle, Effects of a nonuniform current distribution on the kinetic inductance of a thin superconducting film, *J. Appl. Phys.* **45**, 5043 (1974).
- [32] D. Zhu, M. Colangelo, B. A. Korzh, Q.-Y. Zhao, S. Frasca, A. E. Dane, A. E. Velasco, A. D. Beyer, J. P. Allmaras, E. Ramirez, *et al.*, Superconducting nanowire single-photon detector with integrated impedance-matching taper, *Applied Physics Letters* **114** (2019).
- [33] W. Fu, M. Xu, X. Liu, C.-L. Zou, C. Zhong, X. Han, M. Shen, Y. Xu, R. Cheng, S. Wang, *et al.*, Cavity electro-optic circuit for microwave-to-optical conversion in the quantum ground state, *Physical Review A* **103**, 053504 (2021).
- [34] K. J. Blow, R. Loudon, S. J. D. Phoenix, and T. J. Shepherd, *PHYSICAL REVIEW A*, Tech. Rep. (1990).
- [35] J. E. Sipe and M. J. Steel, A Hamiltonian treatment of stimulated Brillouin scattering in nanoscale integrated waveguides, *New Journal of Physics* **18**, 045004 (2016).
- [36] P. Kharel, R. O. Behunin, W. H. Renninger, and P. T. Rakich, Noise and dynamics in forward Brillouin interactions, *Physical Review A* **93**, 063806 (2016).